INTERNATIONAL JOURNAL FOR NUMERICAL METHODS IN FLUIDS
Int. J. Numer. Meth. Fluids 2004; **46**:85–107 (DOI: 10.1002/fld.749)

An immersed boundary finite difference method for LES of flow around bluff shapes

C. W. Li*,† and L. L. Wang

Department of Civil and Structural Engineering, the Hong Kong Polytechnic University, Hong Kong

SUMMARY

A three-dimensional numerical model using large eddy simulation (LES) technique and incorporating the immersed boundary (IMB) concept has been developed to compute flow around bluff shapes. A fractional step finite differences method with rectilinear non-uniform collocated grid is employed to solve the governing equations. Bluff shapes are treated in the IMB method by introducing artificial force terms into the momentum equations. Second-order accurate interpolation schemes for all sorts of grid points adjacent to the immersed boundary have been developed to determine the velocities and pressure at these points. To enforce continuity, the methods of imposition of pressure boundary condition and addition of mass source/sink terms are tested. It has been found that imposing suitable pressure boundary condition (zero normal gradient) can effectively reproduce the correct pressure distribution and enforce mass conservation around a bluff shape. The present model has been verified and applied to simulate flow around bluff shapes: (1) a square cylinder and (2) the Tsing Ma suspension bridge deck section model. Complex flow phenomena such as flow separation and vortex shedding are reproduced and the drag coefficient, lift coefficient, and pressure coefficient are calculated and analyzed. Good agreement between the numerical results and the experimental data are obtained. The model is proven to be an efficient tool for flow simulation around bluff bodies in time varying flows. Copyright © 2004 John Wiley & Sons, Ltd.

KEY WORDS: large eddy simulation; fractional step methods; immersed boundary method

1. INTRODUCTION

Flow past bluff bodies occur in many branches of engineering, such as water flow around hydraulic structures and wind flow around buildings. The resulting flow pattern is usually very complex and highly transient, including flow separation, vortex shedding, high level of turbulence and large scale eddies. The application of computational fluid dynamics (CFD) in this area for the design and testing of technological solutions has received attention in the past two decades. The technique of large eddy simulation (LES) becomes increasingly popular

*Correspondence to: C. W. Li, Department of Civil and Structural Engineering, the Hong Kong Polytechnic University, Hong Kong.
†E-mail: cewli@polyu.edu.hk

Published online 17 June 2004

Received 21 August 2003
Revised 5 April 2004

because it has less empiricism and the excessive computational effort required is relieved by the advancement in computing technology.

To deal with complex geometry, rectilinear grid system is known to be inferior and body-fitted curvilinear or unstructured grid system is frequently used. The latter methods are more complicated in terms of grid generation and solution algorithm and are computationally more expensive. In addition, in many practical problems geometrical complexity is combined with moving or deformable boundaries, which considerably increases the computational difficulties since regeneration of the grid system is required at every time step. Consequently the simulation of flow past bluff bodies using LES technique will be very expensive and time consuming, owing to the large number of nodes, the large number of computing operations per node and the high storage requirements. A numerical procedure that can cope with the flow and geometry complexity but at the same time retain the accuracy and efficiency of the method based on fixed rectilinear grids is highly desirable. One approach that has such advantages is the immersed boundary (IMB) method.

The basic idea of the IMB method lies on the definition of the solid (either moving or not) boundaries. Instead of using complicated boundary fitted grids to define the geometrical configuration, the IMB method actually mimics a solid body by means of suitably defined body forces applied to the discretized set of the momentum equations. The body force is imposed so that the velocity distribution on an immersed boundary is equal to a specified function.

The immersed boundary concept was originally presented in the pioneering work of Peskin [1], who reported at the beginning of the 1970s the simulation of blood flow in heart assuming a low Reynolds number (Re) and two-dimensional flow. Goldstein *et al.* [2] seems to be the first group using this method to treat solid boundaries. The IMB technique was combined with spectral methods to simulate two-dimensional startup flow around a circular cylinder, as well as three-dimensional plane and ribbed-turbulent channel flow. In order to calculate the forcing F, two empirical coefficients related to the flow frequencies were introduced. The forcing F induced spurious oscillations and numerical instability which restricted the computational time step size. Saiki and Biringen [3] used the same forcing as that used by Goldstein to compute the flow around fixed and rotating circular cylinders using a fourth-order central finite-difference scheme. Their results showed that the use of finite difference scheme eliminated the occurrence of spurious oscillations of flow at the boundary.

Mohd-Yusof [4] proposed a direct forcing method which is significantly more stable. In the method no empirical coefficients are required, and the derivation of forcing F is unambiguous. The method has been successfully applied to calculate flows around cylinders and spheres at moderate Re. In the actual implementation of the method, the direct evaluation of the forcing function is unnecessary. This makes the method similar to the ordinary way of imposing the velocity boundary condition. Kim *et al.* [5] introduced both the forcing terms into the momentum equations and the mass source term into the continuity equation to fulfill the continuity requirement at the solid boundary. Their results showed that the errors in the computation for the case with the mass source term were much smaller than those without the mass source term and were comparable to those obtained by the conventional method. Fadlun *et al.* [6] defined F as the forcing acting only on the grid cells with the mimicked boundary. The velocity at the first grid point external to a solid body is obtained by linear interpolation of the velocity at the second grid point (which is obtained by directly solving the N–S equation) and the velocity at the body surface. In Kim's method, the momentum

forcing is applied on the body surface or inside the body. In almost all of the reported works, staggered arrangement of variables on structured rectilinear grids was adopted. Finite volume method (FVM) and finite difference method (FDM) were used to discretize the governing equations.

In the present paper, a 3D LES flow model is developed in which the IMB method is incorporated with a fractional step finite difference scheme. The momentum forcing terms are explicitly evaluated to eliminate empiricism. The flow variables are defined on a collocated grid system which makes the interpolating procedures much simpler and easier to be implemented. The second-order accurate linear or bilinear interpolations are used to estimate the flow variables at the gird points adjacent to the immersed boundary. Zero pressure gradient boundary condition is also incorporated into the interpolation procedures to effectively reproduce the correct pressure distribution on the immersed boundaries and to enforce mass conservation. The model will be validated and applied to the simulation of flows around a square cylinder and the TsingMa suspension bridge deck section model.

2. IMB CONCEPT

The concept of the IMB lies on the definition of the solid boundaries. When 'fluid flows over a body it exerts a normal force on the surface and, if the surface is no-slip, the fluid also exerts a shear force. So the surface exerts a force of opposite sign on the fluid, in the no-slip case, this localize force is what brings the fluid to rest on the body' [2]. The implication is that the effect of certain boundary conditions can be modelled by an external force field rather than by the specification of boundary values. Hence, instead of using complicated boundary fitted grids to define the body in the flow, the IMB method actually mimics it by means of suitably defined body forces applied to the discretized set of momentum equations. The Navier–Stokes equations with such forcing terms introduced through the boundary conditions can be written as

$$\frac{Du}{Dt} = -\nabla p + v\nabla\cdot[\nabla u] + F \tag{1}$$

where $u =$ velocity vector; $p =$ pressure, $v =$ kinematic viscosity, $F =$ body force vector. The body force F should be calculated at every time step so that the velocity distribution on an arbitrary surfaces S is equal to a specified vector function V_S. The body forcing is applied only on the immersed boundary, and sometimes inside the body. When the forcing point coincides with the immersed boundary, the momentum forcing is specified such that the velocity is zero at that point (no-slip condition). For the forcing point inside the body and nearest to the boundary, the momentum forcing is specified such that the normal and tangential velocity components with respect to the boundary are equal and opposite to the velocity components at the corresponding point just outside the body. When the boundary surface does not coincide with a grid plane, the forcing F will act on the points nearest to the immersed boundary. An interpolation method for the forcing will be needed so that the forcing will render the velocity at the immersed boundary exactly equal to V_S.

For the grid point on a boundary S,

$$u^{n+1} = u^n + \Delta t(Rhs + F) = V_s \tag{2}$$

where the superscript n = number of time step; Δt = time step size; Rhs = sum of the pressure gradient, advection and diffusion terms; V_s = specified velocity along the boundary. To make the velocity of the new time step u^{n+1} equal to the desired value V_S on the immersed boundary, the source term F of Equation (1) can be computed by

$$F = -Rhs + \frac{V_S - u^n}{\Delta t} \tag{3}$$

This forcing is direct in the sense that the desired value of the velocity is imposed directly on the boundary without any empiricism.

The main advantage of IMB is that the forcing F can be prescribed on a regular grid and the accuracy and efficiency of the solution procedure on simple rectilinear grids are maintained. In principle there are no restrictions for the velocity distribution V_S. In case of a stationary solid body with no-slip boundary condition, $V_S = 0$ along the boundary, and the implementation of the IMB is much simpler. Also the application of this method to multi-body problem is straightforward [7].

3. GOVERNING EQUATION

The governing equations for the spatially filtered flow are derived from the N–S equations and are written as follows:

$$\frac{\partial u_i}{\partial x_i} = 0 \tag{4}$$

$$\frac{\partial u_i}{\partial t} + u_j \frac{\partial u_i}{\partial x_j} = -\frac{1}{\rho} \frac{\partial p}{\partial x_i} + \frac{\partial}{\partial x_j}(\tau_{ij} + R_{ij}) \tag{5}$$

where x_i $(i = 1, 2, 3,$ and $x_1 \equiv x, x_2 \equiv y, x_3 \equiv z)$ are Cartesian co-ordinates in the streamwise, spanwise and vertical directions, respectively; u_i $(i = 1, 2, 3,$ and $u_1 \equiv u,\ u_2 \equiv v,\ u_3 \equiv w)$ the corresponding velocity components; ρ the density, τ_{ij} the shear stress tensor due to kinematic viscosity, R_{ij} the sub-grid scale shear stress tenor due to spatial filtering.

In the present study, the Smagorinsky model is used to close the sub-grid scale stresses R_{ij}, in which $R_{ij} = \gamma_t S_{ij}$, where S_{ij} is the strain rate tensor of the resolved field, γ_t = eddy viscosity. The eddy viscosity is parameterized by $\gamma_t = 2(L_s^2 \sqrt{2 S_{ij} S_{ij}})$, where L_s is the characteristic length scale $= C_s(\Delta_1 \Delta_2 \Delta_3)^{1/3}$ with Δ_i = grid size in ith direction, $C_s = 0.15$. By incorporating the IMB method, the governing equation (5) can be rewritten as

$$\frac{\partial u_i}{\partial t} + u_j \frac{\partial u_i}{\partial x_j} = -\frac{1}{\rho} \frac{\partial p}{\partial x_i} + \frac{\partial}{\partial x_j}(\tau_{ij} + R_{ij}) + f_i \tag{6}$$

where f_i is the body force component acting on the desired points near the boundary or the points inside the immersed boundary.

3.1. Fractional step method

The fractional step method is used to solve Equations (4) and (6). The entire computational procedure is broken into four major steps: advection step, diffusion step, pressure propagation

step and body force step. The present model is modified from the model by Lin and Li [8] in which the sigma-co-ordinate transformation is used. In the present model the sigma-transformation is still retained so that the model can handle a wide range of problems, such as waves against bluff bodies.

Advection step. The finite difference form for the advection step of the x-momentum equation can be written as

$$\frac{u_{i,j,k}^{n+1/4} - u_{i,j,k}^{n}}{\Delta t} + \left(u\frac{\partial u}{\partial x} + v\frac{\partial u}{\partial y} + w\frac{\partial u}{\partial z} \right)_{i,j,k} = 0 \tag{7}$$

where (i,j,k) = location of a grid point. The method of backward characteristics is employed to solve the above equation. Assume the spatial variation of a function (e.g. velocity component) can be decomposed into a series of Fourier wave components, the schemes in this class of method produce accurate solution for the advection of waves. In particular the phase accuracy is high and the amplitude damping is small. Under uniform grid system the combination of the quadratic backward characteristics method [9] and the Lax–Wendroff method gives the Minimax characteristics method [10]. The implementation of this method to non-uniform grid has been carried out by Li and Lin [11] and the method is adopted here.

Diffusion step. The diffusion process is solved after the advection is completed. The difference form of the diffusion step for the x-momentum equation is

$$\frac{u_{i,j,k}^{n+2/4} - u_{i,j,k}^{n+1/4}}{\Delta t} = \left(\frac{\partial \tau_{xx}}{\partial x} + \frac{\partial \tau_{xy}}{\partial y} + \frac{\partial \tau_{xz}}{\partial z} \right)_{i,j,k}^{n+1/4} \tag{8}$$

where

$$\tau_{ij} = (\gamma + \gamma_t)\left(\frac{\partial u_i}{\partial x_j} + \frac{\partial u_j}{\partial x_i} \right) \tag{9}$$

The second order central difference scheme in space and forward difference in time are used to discretize equation (8).

Pressure propagation step. The pressure propagation step solves the pressure gradient and the additional source and sink terms except the body force term f_i. The projection method has been employed to calculate the pressure and velocity field so that the updated velocity field satisfies the divergence-free condition as imposed by the continuity equation (1). The final Poisson equation for pressure is as follows:

$$\frac{\partial^2 p}{\partial x^2} + \frac{\partial^2 p}{\partial y^2} + \frac{\partial^2 p}{\partial z^2} = \frac{\rho}{\Delta t}\left(\frac{\partial u}{\partial x} + \frac{\partial v}{\partial y} + \frac{\partial w}{\partial z} \right)_{i,j,k}^{n+2/4} \tag{10}$$

There are two commonly used grid system in numerical flow models: collocated grid and staggered grid. In the conventional collocated grid, the solution of the pressure Poisson equation and the satisfaction of the continuity constraint can be problematic due to pressure–velocity coupling and the existence of pressure oscillations. One remedy is to use a fully staggered arrangement of the velocity components and pressure variables. However, the discretization of the cells near the immersed boundary will then be complicated. Another way is still using the collocated grid, but with the pressure derivatives evaluated at the cell face locations by linear interpolation [12]. This results in the standard second order central difference discretization

of the second order pressure derivatives. This scheme will eliminate any 1Δ oscillation in pressure if the source terms in the Poisson equation are evaluated at the cell surfaces by linear interpolation. The scheme is not exactly energy conserving because the evaluation of the source terms at the cell interfaces introduces a second order error term proportional to the fourth order to the pressure gradient. However, this term is small and is of the same order as the error in the basic discretization scheme and so does not affect significantly the overall accuracy of the scheme. In a previous numerical study of wave propagation problem [8], the energy decay is found to be less than 2%.

In the present study the collocated grid is used, and the velocity and pressure derivatives are evaluated at the cell face locations by linear interpolation to eliminate pressure oscillations. The main advantage of the present approach is that the grid system is very simple, and the numerical scheme including the interpolation procedure for boundary grid points is easier to be implemented.

One of the main challenges in the simulation of flows with geometrically complex domain is the search of an accurate and fast solution algorithm for pressure, since the solution for pressure is the most computationally intensive step in the whole solution. In the present work a stable and robust conjugate gradient method CGSTAB [13, 12] is adopted to solve the above equation.

The updated velocity can then be calculated by the velocity correction equations

$$u_{i,j,k}^{n+3/4} = u_{i,j,k}^{n+2/4} - \frac{\Delta t}{\rho}\left(\frac{\partial P}{\partial x}\right)_{i,j,k}^{n+2/4} + \Delta t \cdot g_x \tag{11}$$

The solution of the momentum equations in y and z directions can be obtained similarly. The full details of the numerical technique can be found in Reference [8].

Body force source step. The IMB method is introduced in this step. The equation is given by

$$\frac{u_{i,j,k}^{n+1} - u_{i,j,k}^{n+3/4}}{\Delta t} = f_i \tag{12}$$

In some reported works [14, 4], the forcing term f_i was not explicitly specified at the grid points adjacent to a solid boundary, so the implementation of the IMB concept is similar to the direct imposition of no-slip boundary conditions used in common models. In the present study, f_i is explicitly calculated as an independent fractional step using the velocity at the previous sub-step and the velocity boundary condition V_s.

3.2. Interpolation method

The major difficulty in using IMB method is the location of the immersed boundary and the imposition of boundary condition at the immersed boundaries. In particular, since the immersed boundary can cut through the underlying Cartesian mesh in an arbitrary manner, the main challenge is to construct a boundary treatment method which will not affect the accuracy and the conservation property of the underlying numerical solver. In the present study, we have developed an automatic boundary location method which is well suited for immersed boundary with an arbitrary shape.

The key boundary co-ordinates of an arbitrary bluff body as shown in Figure 1(a) are firstly input into the model. The shape is fixed in the regular grid system by two sets of nodes marked

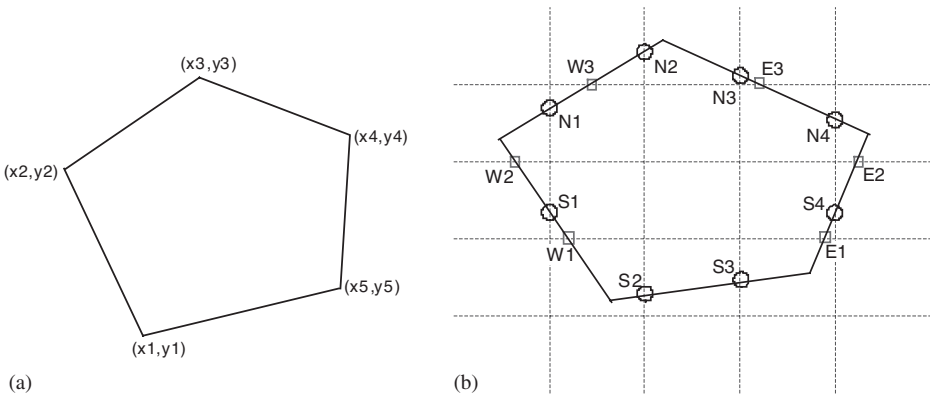

Figure 1. Grid point identification of an arbitrary bluff shape: (a) arbitrary bluff shape; and (b) positioning of the bluff shape.

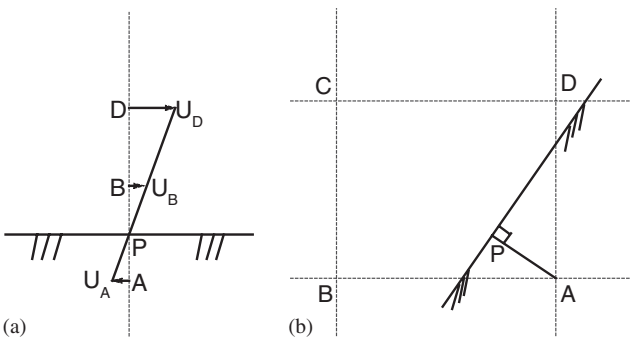

Figure 2. Schematic diagrams for the interpolation scheme: (a) linear interpolation; and (b) bilinear interpolation.

in Figure 1(b) as E(east), W(west) and S(south), N(north). According to the co-ordinates of these nodes, all the grid points in the computational domain can be identified automatically by 0 for the interior points, 1 for external points and 8 for the points on the immersed boundary. If the position of the immersed boundary is time varying or the body is deformable, the only extra effort is to work out the time-varying immersed boundary co-ordinates in Figure 1(a). In this case, the markers of grid points will be identified automatically at every time step and the time-varying immersed-boundary can be simulated without any technical difficulties.

For the nodes located exactly on the immersed boundary, f_i can be calculated easily from Equation (12). Obviously this is not always the case when the immersed boundary has complex shape. Therefore, an interpolation procedure is required. In the present study, the second-order linear or bilinear interpolation procedure for the velocity is used. Figure 2 shows the schematic diagrams for the interpolation schemes used in this study. In Figure 2(a), P is the point on

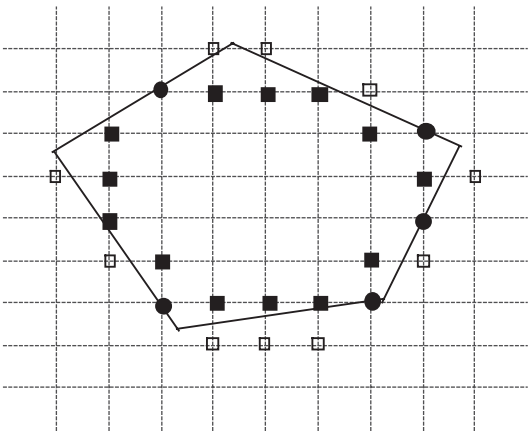

Figure 3. Nodes for non-zero forcing (filled squares and circles).

the immersed boundary for which the no-slip boundary condition should be satisfied, and A is the nearest interior point which has only one fluid neighbour point (node B). In this case, U_A and U_B is obtained by linear interpolation between U_D and the no-slip velocity condition at P.

$$U_A = -\frac{h_a}{h_d} U_D, \quad U_B = \frac{h_b}{h_d} U_D \tag{13}$$

where, h_a, h_b, h_d are the distances between A, B, D and P, respectively. Certainly this interpolation method requires the grid to be fine enough closed to the boundary so that the interpolated velocity is accurate. Comparison with the interpolation methods proposed by Kim *et al.* [5], the present approach, Equation (13), gives a more realistic velocity distribution because a virtual no-slip velocity condition has been satisfied between nodes A and B. In Figure 2(b), the interior point A has two fluid-neighbour nodes B and D. By using the second-order bilinear interpolation, we have

$$U_P = \frac{[(U_D \cdot \Delta x_1 + U_C \cdot \Delta x_2)\Delta y_2 + (U_A \cdot \Delta x_1 + U_B \cdot \Delta x_2)\Delta y_1]}{[(\Delta x_1 + \Delta x_2)(\Delta y_1 + \Delta y_2)]} \tag{14}$$

where $\Delta x_1 = x_P - x_B$, $\Delta x_2 = x_A - x_P$, $\Delta y_1 = y_D - y_P$, $\Delta y_2 = y_P - y_A$. By setting $U_P = 0$, U_A can be calculated from Equation (14). This scheme can also be used to obtain the interpolated values of the pressure at point P.

According to the definition of momentum forcing, non-zero force exists only at the immersed boundary or at the points inside the immersed boundary, such as the filled black points in Figure 3. The points with hollowed marks are the only fluid-neighbour nodes at the interior of the closed boundary. The velocity at these points will also be changed when the interpolation equation (13) is used. So a non-zero momentum forcing on these points will be obtained by Equation (12).

The other interior points in Figure 3 are the 'dry' or 'inactive' points. There are two different ways to treat these points [6]:

(a) Impose the forcing on the interior points without any smoothing; this is equivalent to the specification the velocity distribution inside the body with the pressure adjusted accordingly;
(b) Leave the interior points free to develop a flow without imposing anything. The flow pattern inside the body will be different from that in case (a), but the external flow will be unchanged.

Both approaches have been tested. The result shows that the external flow is essentially independent of the internal flow conditions. In the present study, we adopted the first approach and impose a zero-velocity distribution in the interior region.

3.3. Boundary condition

A uniform current or a linear wave can be imposed at the inflow boundary of the computational domain. All the variables will be specified based on analytical solution or experimental measurement. At the outflow boundary, the radiation condition is used for all the variables. The pressure is zero at the free surface and the vertical gradients of all the velocity components are zero. At the bottom the velocity components in the normal and tangential direction are zero (no-slip), and the vertical gradient of pressure is balanced by the gravitational acceleration.

3.4. Mass conservation and pressure boundary condition

Kim *et al*. [5] introduced a mass source/sink, q, for the cells containing the immersed boundary to satisfy local mass conservation. The continuity equation was written as

$$\frac{\partial u_i}{\partial x_i} - q = 0 \tag{15}$$

in which q was applied only on the boundary or inside the enclosed boundary. Their numerical results showed that the mass source/sink term was essential in order to obtain a realistic solution and to increase the accuracy of the solution near boundary. On the other hand, Fadlun *et al*. [6] postulated that the pressure boundary condition could be automatically satisfied at the immersed boundary with no mass source term introduced in the governing equations.

Obviously, if no treatment is applied, the local continuity of the flow adjacent to the immersed boundary may not be satisfied, especially at the beginning of the simulation when incorrect initial condition is used. While after adding the mass source in the cells containing the immersed boundary, global mass within the computational domain may not be conserved.

If the internal flow pattern is independent of the external flow as mentioned above, the mass source/sink will affect only the interior flow pattern and the flow closed to the boundary. In the present study, flows around cylinder for both cases with and without mass source/sink term are tested. We found that in both cases, although the velocity satisfies the no-slip boundary condition along the immersed boundary, the calculation is not quite stable since the pressure distribution is incorrect near the immersed boundary. The problem is alleviated by the imposition of zero normal gradient condition of pressure. This approach can be interpreted as an

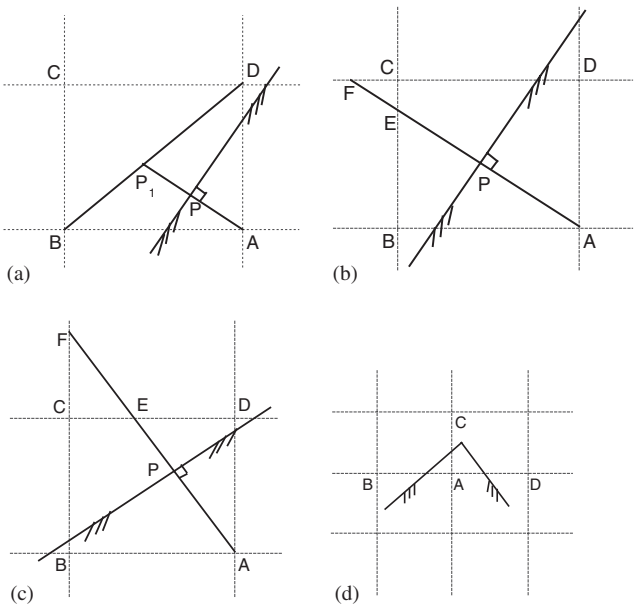

Figure 4. Implementation of the zero gradient pressure condition: (a) two fluid neighbour nodes; (b) one fluid neighbour node; (c) one fluid neighbour node; and (d) three fluid neighbour points.

alternative way to enforce continuity since the Poisson equation is derived from the continuity equation. It is easy to understand that when $P_A = P_B$ in Figure 2(a), mass conservation at point P will be satisfied automatically since there will be no flow across the boundary. In our view, specifying pressure at the boundary can effectively reproduce the correct pressure distribution and enforce continuity.

The implementation of zero gradient pressure condition is illustration in Figure 4. In Figure 4(a), node A has two fluid neighbour nodes B and D, zero normal pressure gradient condition on point P can be obtained by setting $p_A = p_{P1}$. In Figure 4(b) and 4(c), node A has only one fluid neighbour node, and the condition can be satisfied by setting $p_A = p_E$. The values p_{P1}, p_E can be calculated by linear interpolation. Pressure of the node which has three fluid neighbour nodes as shown in Figure 4(d) is set as the average of the pressure values at the three neighbour points, $p_A = (p_B + p_C + p_D)/3$.

Linear interpolation method is employed to calculate the unknown pressure, and the results will generally have second order accuracy. However, the grid spacings in different directions are better to be of similar size for the method to be easily implemented.

4. FLOW AROUND SQUARE CYLINDER

The flow around a cylinder frequently occurs in various internal and external engineering flow problems such as wind engineering, hydraulic engineering and heat transfer problems. Various experimental and numerical studies have been conducted on the flows around square

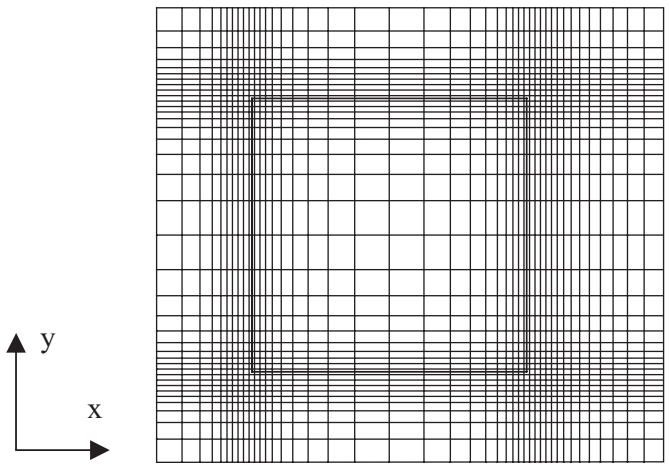

Figure 5. Mesh arrangement near the cylinder (only every other grid line is shown in both directions for better visibility).

cylinders because the orthogonal geometrical configuration of the cylinder can be treated with relatively simple grids and, on the other hand, some typical complex flow phenomena such as separation, vortex shedding, wake formation and growth behind the body will occur. This problem is used in the present study as the first test case.

In the computation the Cartesian co-ordinate system is used. The x-axis is aligned with the inflow direction. The z-axis is parallel with the vertical axis of the cylinder and perpendicular to the horizontal (x, y) plane. The square cylinder of dimension $0.1\,\mathrm{m} \times 0.1\,\mathrm{m} \times 0.1\,\mathrm{m}$ is deployed in a channel that measures $2.0\,\mathrm{m} \times 1.0\,\mathrm{m}$ in x, y direction, respectively. The still water depth is 0.1 m. The cylinder is located at the centre along the y direction and its front face is at a distance 0.55 m from the inlet boundary. The incoming channel flow has a uniform velocity of 0.22 m/s. No artificial velocity fluctuation is introduced at the inflow boundary. The Reynolds number in this case is estimated to be $Re = UL/\gamma = 2.2 \times 10^4$, where U is the velocity of incoming flow and L is the width of the cylinder. The value of Re in this study is the same as that used in the experimental study by Lyn *et al.* [15], based on which Yu [16], Rodi [17], Li and Lin [11] validated their numerical models.

A non-uniform mesh is employed, which has a total number of 150×108 grids on the horizontal plane with the finest grid $\Delta x = \Delta y = 0.001\,\mathrm{m}$ (equal to 1% width of the cylinder) arranged near the four corners of the cylinder (Figure 5). A total of 20 uniform grids are used in the vertical direction. Grid size ratio (ratio of the adjacent grid sizes) is 1.0–1.2 in x, y direction and 1.0 in z direction. Dynamic time step Δt is determined by the stability criteria based on the Courant number and the non-dimensional diffusion number. A time step of $\Delta t = 4 \times 10^{-4}$ s is used to carry out the computation up to $t = 35$ s. The computer cost is approximately 6.4 CPU s/time step with a grid of approximately 3.6×10^5 nodes, running on a Pentium 4 PC with 2.4 GHz CPU. In fact, apart from the numerical method used, RAM and CPU requirements of a computer code depend on many other factors, such as the computer programming technique in writing the code, the output requirement, and hardware architecture of the computer systems.

The governing equations on all the points that correspond to the internal *fluid* part of the domain have been solved. The stability and accuracy of the calculation depends on many factors such as flow velocity, turbulence model, numerical method, the geometry to be mimicked and grid size. In the computation it is found that the most important factor is the grid size and its ratio in different directions near the boundary of the cylinder. When the grid size $\Delta x = \Delta y = 0.004$ m is used, the computed results display no separation phenomena on the two side surfaces of the cylinder and vortex shedding is limited in a small region behind the cylinder. And the use of large ratio of grid sizes in different directions may cause incorrect interpolation results. Both cases with and without mass source/sink are tested and the results display not much difference. We will present the results and discussions for the case without mass source term unless otherwise indicated.

4.1. Vortex shedding

It is well known that when Re is high enough, the flow passing a bluff body will become turbulent and vortices will be formed at the separation points that are generally located at the sharp corners if exist. Normally, the shedding is periodic and the shedding frequency f depends on both the incoming flow and the size and shape of the solid body. In the present study, the inflow is basically laminar, with $Re = 2.2 \times 10^4$. The flow around the square cylinder will experience the states from symmetric flow to separation at the front corners and vortex shedding behind the cylinder. All these phenomena have been observed in the computed results. Before the fully developed state is achieved, the transient period lasts about 13 s. Figure 6 displays the contours of vorticity at different time. From the figure we can see clearly that at the initial stage, the flow is basically symmetric about the centreline of the cylinder in y-direction. As time elapses, it becomes asymmetric and chaotic. From 8.0 s onwards, vortex shedding occurs in an unstable way at about one unit (0.1 m) downstream from the back face of cylinder. This process can be regarded as the evolution from laminar flow to fully developed turbulent flow and reach the dynamic steady state eventually.

After 13 s, the periodic vortex shedding phenomenon becomes stable. Figure 7 shows the contour plots of vorticity from 14.4 s to 18 s during which about one vortex shedding cycle is completed. It is seen that the vortices are originated from the front corners of the cylinder and carried over the back corners and eventually becomes periodic. The position of the shedding is much closer to the back face of the cylinder comparing with the previous state and vortex shedding occurs in a long downstream distance. Non-dimensional parameter that is related to the frequency of vortex shedding is defined by, $St = fL/U$, which is commonly referred to as the Strouhal number. In the study the shedding period is found to be about 3.42 s, and $St = 0.133$ which is in very good agreement with the value of 0.13 obtained from experiment [18] and most of the numerical computations [17].

4.2. Pressure field

In Figure 8, the computed distribution of the mean pressure coefficient around the cylinder is compared with the experimental data and other numerical results. The pressure coefficient C_p is defined by $C_p = (p - p_0)/0.5\rho u_0^2$, where u_0 is the uniform velocity at the inflow boundary, p_0 the undisturbed pressure, p the mean pressure. The current simulation results are in good agreement with the experimental data except at two points at the front corners of the cylinder.

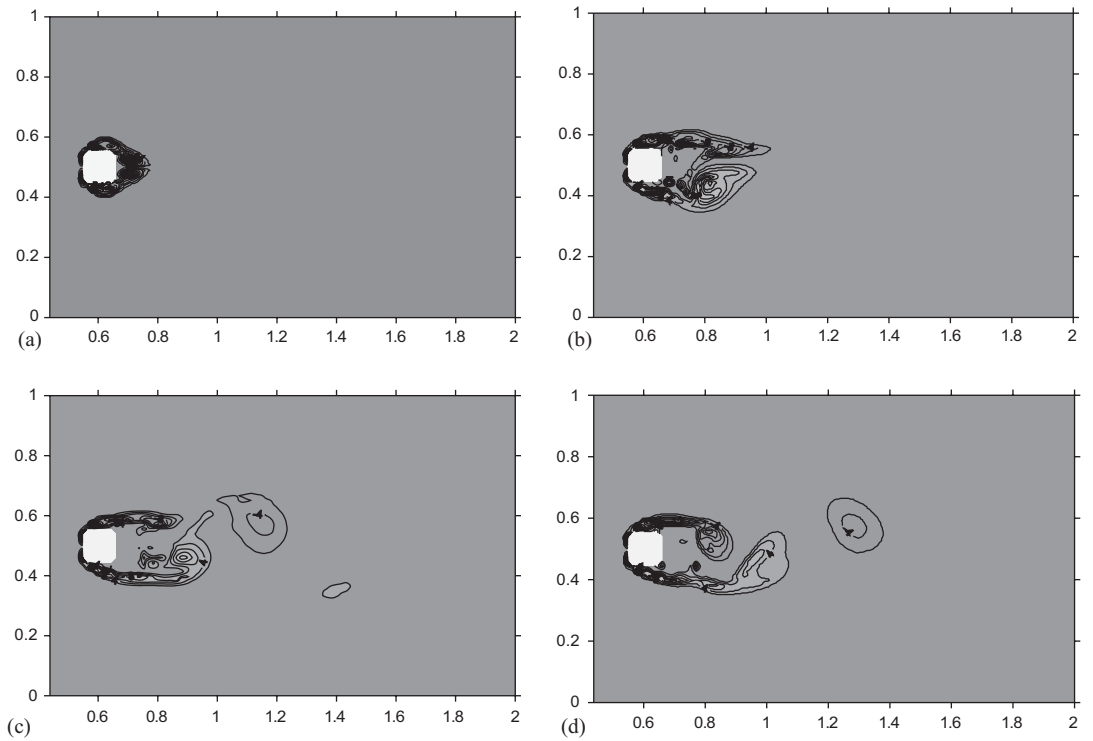

Figure 6. Contour plots of the vorticity at different time: (a) 1.2 s (symmetric structure); (b) 5.0 s (chaotic structure); (c) 8.8 s (unstable shedding); and (d) 9.6 s (unstable shedding).

The results are better than the numerical results by using the normal 3D LES model (the experimental data of Lee [19] did not give out the pressure coefficients at the four corner points). The pressure coefficient $-C_{pb}$ on the leeward face is around 1.484 which is within the range of the experimental values of 1.3–1.6 (see Table I).

4.3. Force coefficients

Force coefficients have important application in the design of hydraulic structure subjected to water flow or buildings subjected to wind blow. In this study, the time histories of force components in x and y directions are calculated by integration of the pressure around the cylinder. The results show that both force components Fx and Fy are of the same order of magnitude and Fx has fairly constant values with small amplitude of oscillation after 13 s, while Fy oscillates strongly due to periodic vortex shedding from the front corners of the cylinder and the period of oscillation is the same as the period of vortex shedding.

The non-dimensional drag force coefficient is defined by $C_{\mathrm{D}} = F_x/(0.5\rho A u_0^2)$ where A is the projected area of the cylinder on a plane perpendicular to the x axis. The lift force coefficient is defined similarly by $C_{\mathrm{L}} = F_y/(0.5\rho A u_0^2)$. The time history of the drag force coefficients C_{D} and the lift force coefficients C_{L} are shown in Figure 9. Table I lists the computed flow parameters and their comparison with the experimental results and other numerical results.

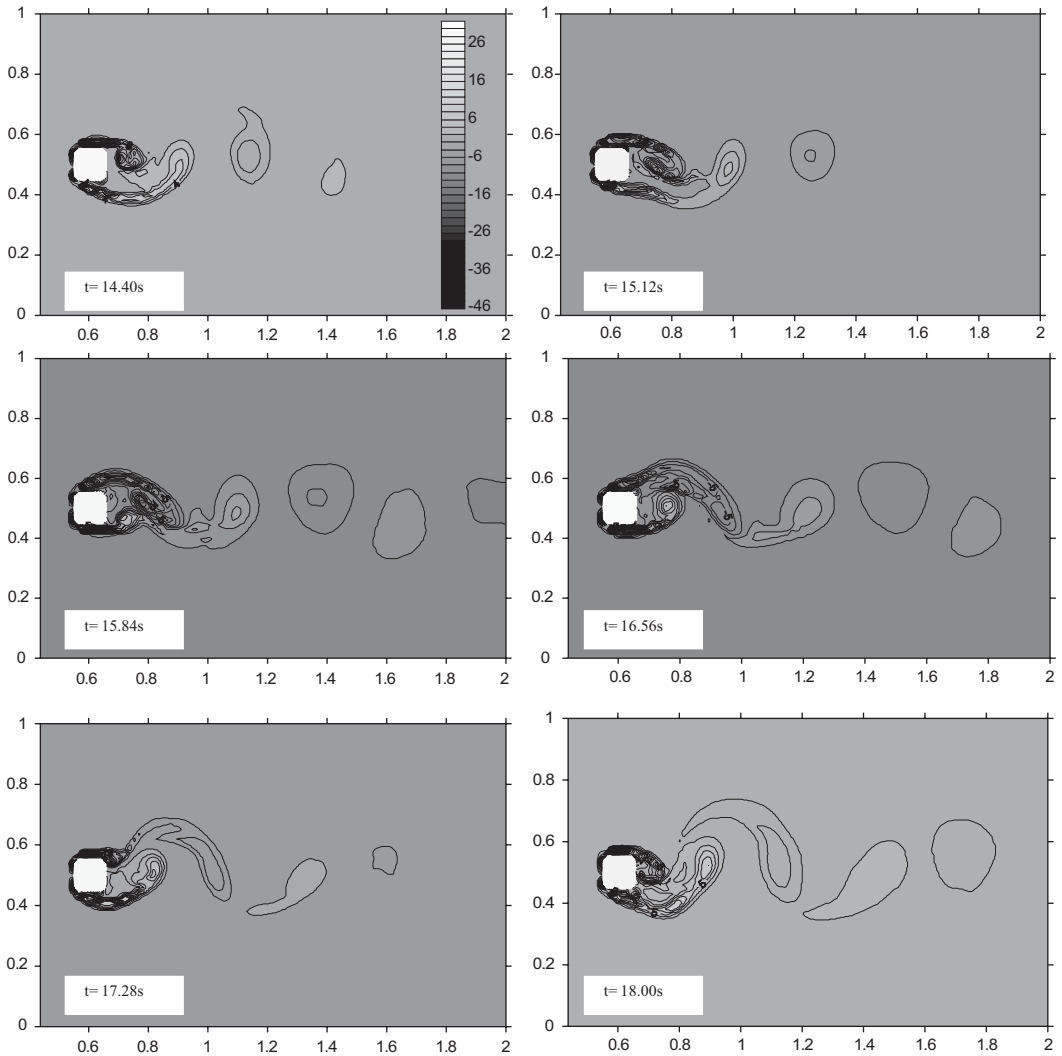

Figure 7. Contour plots of vorticity for stable vortex shedding within one period.

The experimental results for the mean drag coefficient are in the range of 2.0–2.16 over a wide range of Reynolds number. The mean drag coefficient for the present study is about 6–7% higher than the upper bound of the experimental results of 2.16. Rodi [17] reported that the simulations used no-slip boundary conditions on solid boundary produced a higher drag coefficient than those used a wall function boundary condition. In the IMB method the no-slip boundary condition is used generally and is adopted in the present study. The experimental results for the root mean squares (RMS) values C'_D and C'_L display considerably variations. The ranges of the experimental obtained coefficients are $C'_D = 0.17 - 0.23$, $C'_L = 0.5 - 1.32$, and the ranges of the previously computed coefficients are $C'_D = 0.1 - 0.27$, $C'_L = 0.38 - 1.79$.

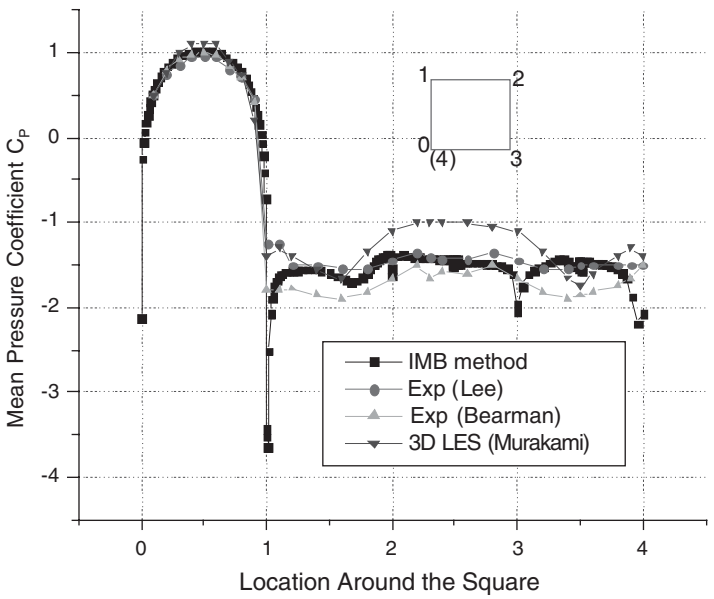

Figure 8. Distribution of the mean pressure coefficient around a square cylinder.

Table I. Summary of the major flow parameters obtained experimentally and numerically.

	$\frac{Re}{1000}$	S_t	$-C_{pb}$	C_D	RMS of C_D C'_D	RMS of C_L C'_L
IMB	22	0.135	1.48	2.32	0.18	1.20
		(0.133)	(1.49)	(2.30)	(0.22)	(1.39)
Rodi [20]	22	0.066–0.14		1.66–2.77	0.1–0.27	0.38–1.79
Yu and Kareem [16]	22	0.135	1.02	2.14	0.25	1.15
Experiments						
Lee [19]	176	0.122	1.30	2.04	0.23	1.23
Bearman and Obasaju [18]	5.8–32	0.130	1.60			1.20
Norberg [21]	13	0.130	1.43	2.16		
Cheng *et al.* [22]	22			2.0		0.5
Vickery [23]	100	0.118	1.32	2.05	0.17	1.32
Lyn *et al.* [15]	21.4	0.132		2.1		

Note: data in bracket are for the case with mass source/sink term.

The presently computed value of C'_D is within the range of experiment results while the computed value of C'_L is at the lower bound of the range of the experimental data. The results show that the RMS coefficients are more sensitive than the mean values to various numerical and physical factors, such as the SGS models, grid layouts, boundary conditions and flow parameters such as the turbulence intensities of the incoming flow, values of *Re*.

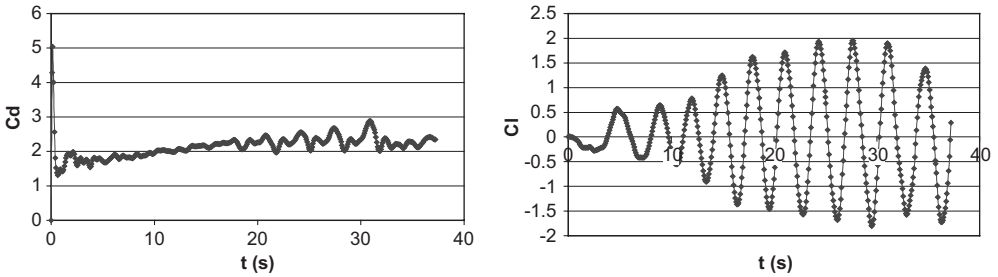

Figure 9. Time histories of the computed normal and transverse force coefficients.

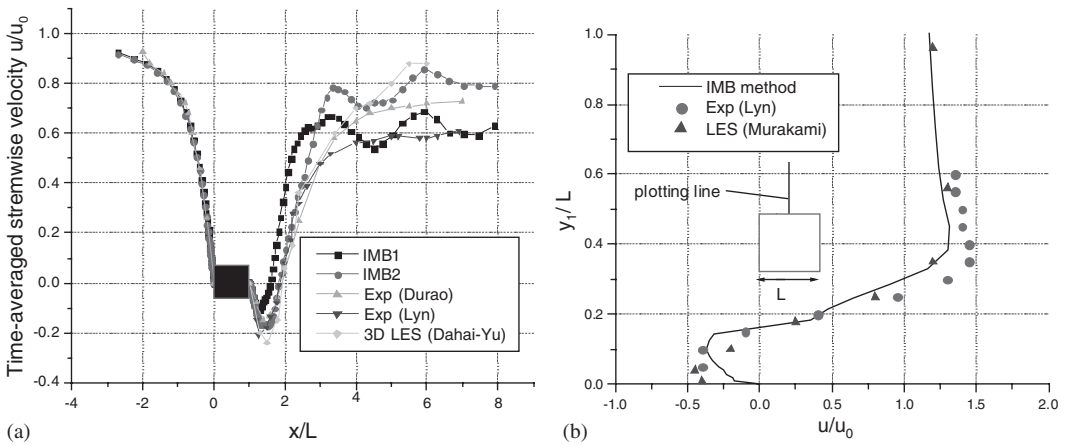

Figure 10. Time-averaged streamwise velocity distribution: (a) along the longitudinal centerline; and (b) along the transverse centreline.

4.4. *Velocity field*

The time-averaged streamwise velocity along the centre line in the x-direction is shown in Figure 10(a) together with the experimental results by Lyn *et al.* [15] and Durao *et al.* [24]. In the figure IMB1 and IMB2 denote the results obtained from the schemes with and without the mass source/sink term, respectively. The displayed results are time-averaged over one shedding period. They are in good agreement with the experimental results in the line segment upstream of the cylinder, and display a faster flow recovery in the wake region. Large scale wiggles are observed from $x = 2.5$L to 6L. These wiggles are suspected due to the effect of the free surface. The asymmetry in the surface and bottom boundary conditions may produce a stronger three-dimensional motion and the steamwise velocity oscillation.

The velocity distribution along the line normal to the side wall of the square cylinder is shown in Figure 10(b), together with the experimental data by Lyn *et al.* and the numerical results by the LES model of Murakami and Mochida [25]. In the present study, the finest grid near the cylinder is L/100, which is the same as that used in the work of Murakami and Mochida. By using the no-slip condition, the velocity shows a clear tendency to approach zero at the wall surface. The reverse flow region is observed clearly. The velocity profile

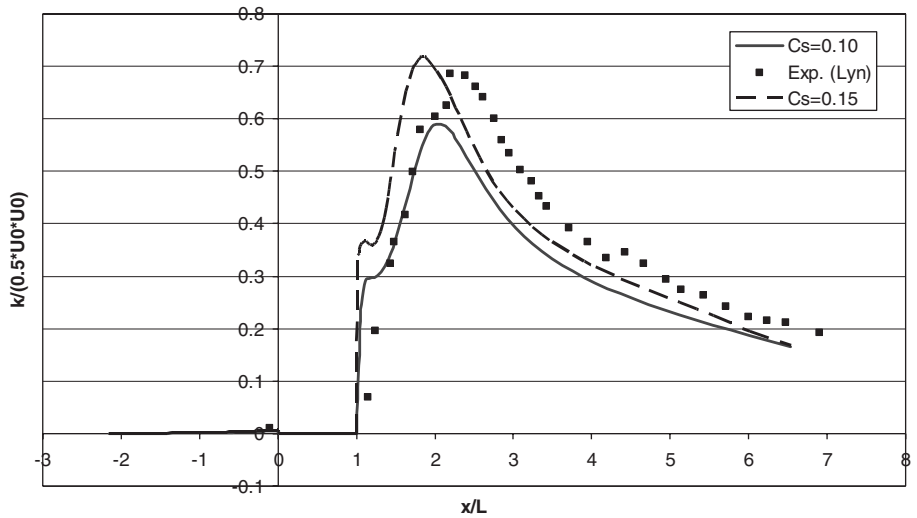

Figure 11. Total fluctuation energy (periodic+turbulent) of velocity along the longitudinal centerline.

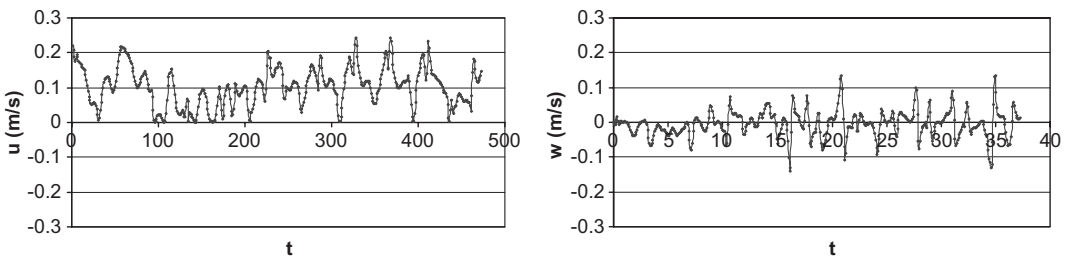

Figure 12. Velocity components u and w at the point (0.8 m, 0 m, 0.05 m).

outside the boundary layer is in good agreement with the numerical results from Murakami and Mochida. It is likely that the large negative velocities close to the side walls of the cylinder will cause higher pressure suction near the upstream corner, and this will result in a larger recirculation region.

Figure 11 displays the total fluctuation energy (periodic plus turbulent) of velocity along the longitudinal centerline. The agreement between the computed results and the measured data is satisfactory. The effect of variation of the value of Smagorinsky constant Cs can be observed here. By reducing the value of Cs form 0.15 to 0.10, about 20% reduction in the peak total fluctuation energy is obtained. The results justify the use of a higher value of Cs of 0.15. The effect of Cs on mean velocities is less apparent.

In Figure 12, the time history of velocities at the point (0.8 m, 0 m, 0.11 m), which is 8L downstream of the front face of the cylinder, is plotted. It can be seen that the vertical velocity w fluctuates around $w = 0$ with the same order of magnitude as that of the streamwise velocity. It shows that the flow field behind the cylinder is indeed three-dimensional although

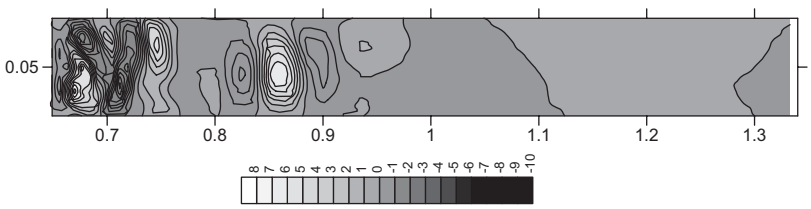

Figure 13. Vortex structure at the vertical symmetric plane and behind the cylinder.

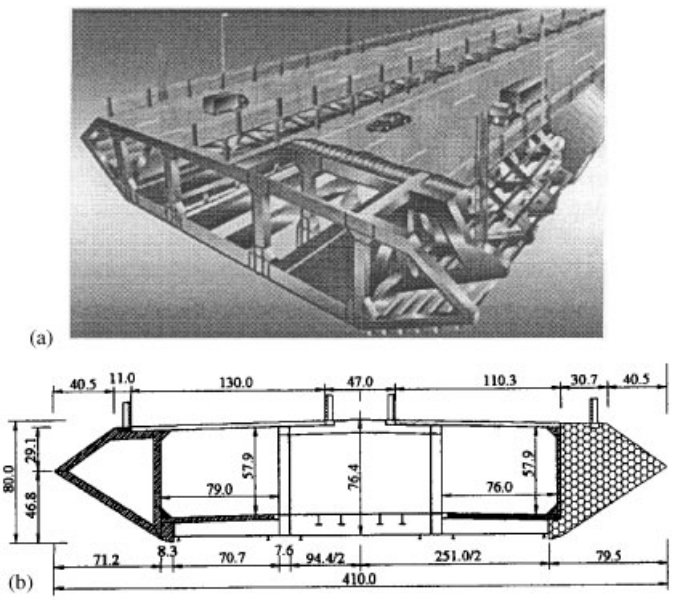

Figure 14. Tsing Ma suspension bridge deck: (a) schematic diagram; and (b) cross section.

the inflow is laminar. There are lots of irregular turbulent vortical structures exist at the middle x–z plane of the cylinder (Figure 13), although the vorticity is only about one sixth of that on the horizontal plane. Instead of having clear downstream movement as time elapses, these vortices seem to generate and disappear stochastically.

5. FLOW AROUND THE TSING MA BRIDGE DECK SECTION MODEL

To further test the IMB method, the simulation of skew flow around a more complex bluff shape, the Tsing Ma bridge deck section model, is carried out. The Tsing Ma suspension bridge deck is a double layer deck, with two railways and two carriage-ways on the lower level within the bridge deck. The dimension of a typical deck section is 41.0 m wide and 7.643 m high (Figure 14). In the present study the geometric scale of the deck sectional model is set at 1:100. This is mainly because LES is still with difficulty in simulating flow with very

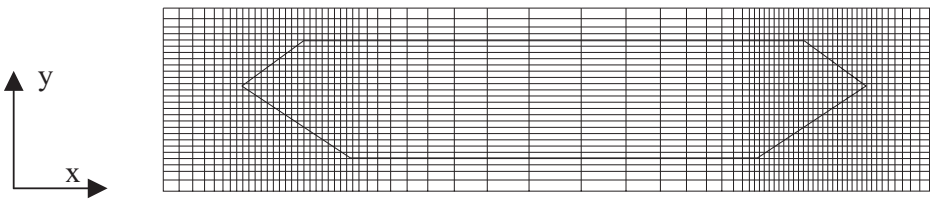

Figure 15. Mesh arrangement near the deck (grid lines are plotted every two grid nodes for better visibility).

large *Re*. In addition the flow patterns are likely to be similar over a wide range of *Re* since the separation points will be always at the sharp corners. The width and height of model are 0.41 and 0.0764 m, respectively while the length is 1.06 m. A computational domain with the length of 7 m in x-direction, 1.0 m in y-direction and 1.06 m in z-direction, is discretized by a non-uniform $276 \times 126 \times 20$ grid system (Figure 15). The centre point of the bridge deck section is located at (2.0 m, 0.5 m) in the horizontal plane. The finest grid in the front and rear part of the deck is 1.6 mm in x direction. Uniform grid with $\Delta y = 2.0$ mm is used in the deck region in y direction. A uniform wind speed u_0 is sent from the left inflow boundary. The air density $\rho_0 = 1.225\,\mathrm{kg/m^3}$ and viscosity $\gamma = 1.0 \times 10^{-5}\,\mathrm{m^2/s}$. A total of five cases have been simulated, with $u_0 = 0.5 - 0.75$ m/s, $Re = 3280 - 5730$. The angle between the mean flow direction and the longitudinal axis, θ, varies from 0 to 5°. The time step $\Delta t = 2.25 \times 10^{-4}$ s which satisfies the numerical stability constraint is used to carry out the computation for 14.0 s.

5.1. *Vortex shedding*

The computed results show that for all cases stable vortex shedding occurs after about $t = 3$ s. Figure 16 displays the vorticity contours of the flow around the bridge deck section for cases of $u_0 = 0.5$ m/s, $\theta = 5°$ and 0°. For the case with $\theta = 5°$, an obvious asymmetric vorticity field is observed, and strong shear stresses on the front section cause flow separations along the upper and lower surfaces. The periods of vortex shedding are mainly determined by wind speed at the inlet boundary, and are insensitive to the rotational angle θ. In this study, the shedding periods are found to be 0.62 and 0.94 s for the cases of $u_0 = 0.75$ m/s and $u_0 = 0.50$ m/s, respectively. These give $S_t = 0.164$ and 0.163 for the two cases. In fact St is approximately constant for all the cases tested.

5.2. *Velocity field*

Figure 17 shows the vector plots at different times within one vortex shedding period for rotation angle $\theta = 0°$ and 5°. It can be seen that the flow pattern behind the deck is basically similar for different rotational angle. The size of the recirculation region is however larger when the rotational angle is not zero. Flow separation can be clearly observed along the upper surface of the deck.

5.3. *Force coefficient*

The total forces in x and y directions are calculated by integrating the pressure around the deck. The time histories of F_x and F_y are given in Figure 18. The results show that both

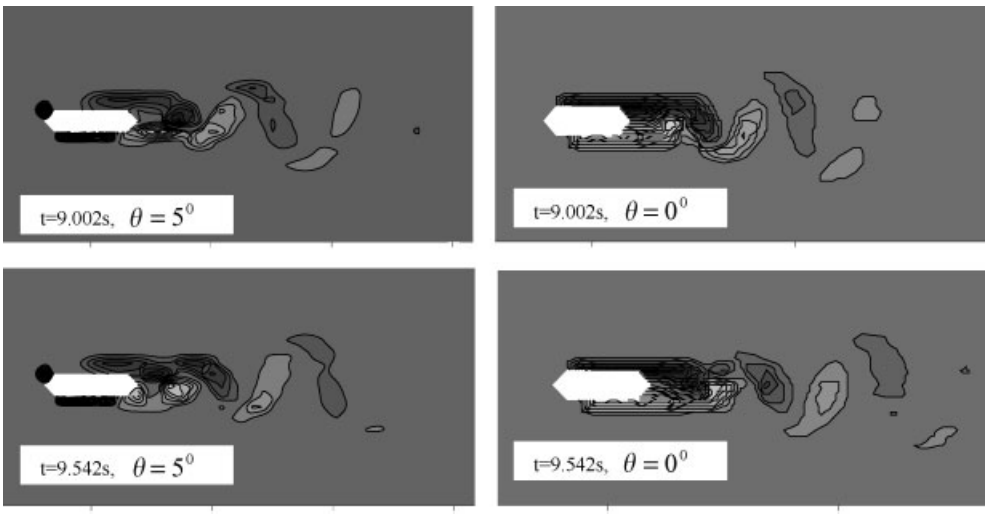

Figure 16. Plots of vorticity contours of the flow around deck for the case of $u_0 = 0.5\,\mathrm{m/s}$ (light colour represents positive vorticity and dark represents negative vorticity).

Table II. Computed force coefficients and Strouhal number.

	$\theta = 0^\circ$	$\theta = 3^\circ$	$\theta = 5^\circ$
C_D	0.4925	0.5570	0.6761
C'_D	0.0330	0.0340	0.0299
C_L	0.0470	0.2710	0.3658
C'_L	0.0270	0.0263	0.0292
S_t	0.163	0.163	0.163

F_x and F_y are of the same order of magnitude and increase with the flow velocity and the rotation angle. F_x is fairly constant after about $t = 3\,\mathrm{s}$ for all cases. F_y is periodic in time due to vortex shedding. The oscillation of F_y is not symmetrical about the axis of $F_y = 0$ as that observed in the case of square cylinder, which is due to the asymmetry of the deck section.

The mean drag and lift coefficients and the RMS coefficients are listed in Table II. The results show that the drag coefficient moderately increases with the rotation angle, and the lift coefficient significantly increases with the rotation angle. The magnitude of the drag or lift coefficients of the bridge deck section is much smaller than that of a square cylinder. This is because the shape for the bridge deck section is closer to a streamline body.

Although there is no detailed experimental data for verification, the computed results are consistent with the general results on flow around bluff bodies, including the correct trend of the force coefficients with the rotation angle, and small force coefficients. The case study shows that the IMB method can be used at least in a comparative study of the effect flows around complex bluff body.

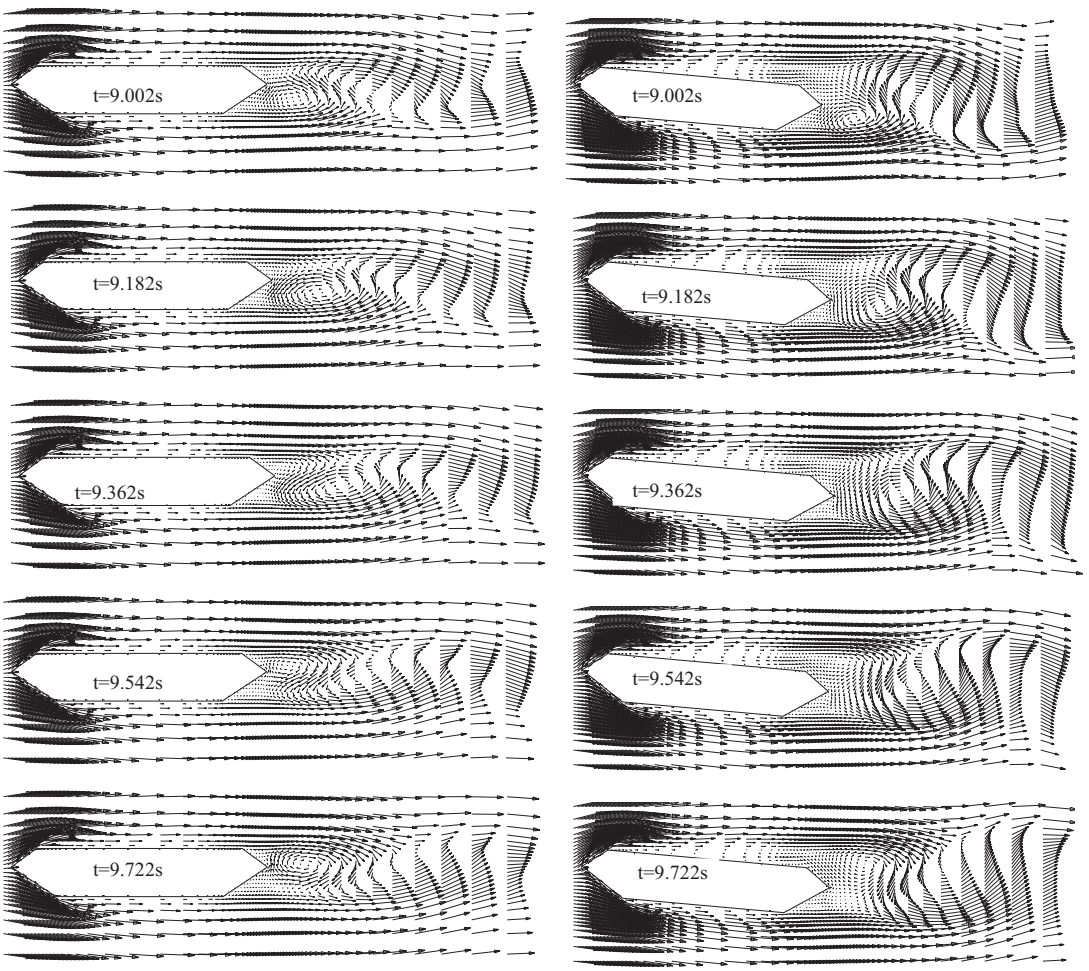

Figure 17. Vector plots at the central x–z plane ($u_0 = 0.5$ m/s, $\theta = 0°$, $5°$; vectors are plotted for every two grid nodes in both x and y directions).

6. CONCLUSIONS

Incorporating the IMB concept with a fractional step FD scheme on collocated grid system, a 3D LES flow model is developed and tested by two cases of flow around bluff shapes: (a) a square cylinder and (2) the Tsing Ma suspension bridge deck model section. The artificial body forcing is explicitly evaluated to satisfy the flow conditions at the immersed boundary. An interpolation method of pressure and velocities at grid points closed to boundary is developed, which is easily implemented due to the use of collocated grid. The results show that the explicit imposition of zero gradient pressure boundary condition along the immersed boundary can effectively reproduce the correct pressure distribution there, enforce mass conservation and improve numerical stability. And the effectiveness of the IMB method in dealing with complex geometry is due to the implementation of the interpolation procedure.

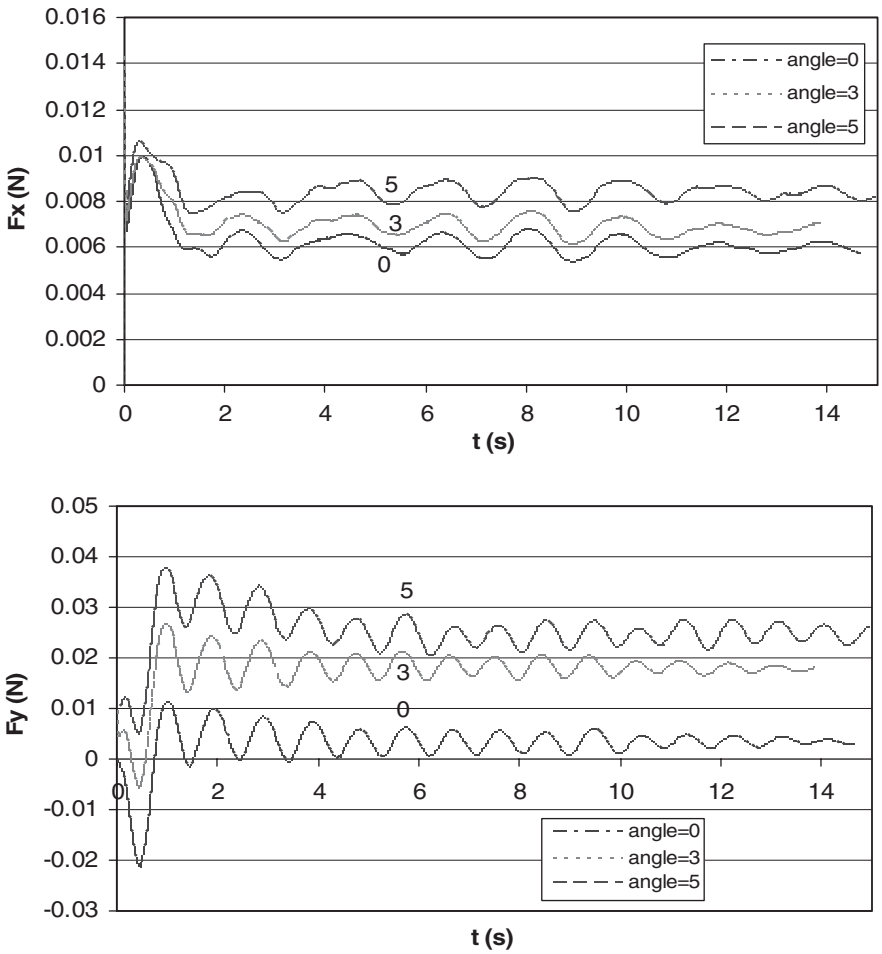

Figure 18. Time histories of the drag and lift forces.

In the case of flow around square cylinder at $Re = 22\,000$, complex flow phenomena such as flow separation and vortex shedding are reproduced. Very good agreement with the experimental data is obtained for almost all the numerical results (flow patterns, drag, lift and pressure coefficients). For flow around the Tsing Ma bridge deck section model, the period of vortex shedding is mainly determined by the approach velocity and the Strouhal number is about 0.16. The relative position of the deck to the flow direction has significant effect on the lift coefficient and the size of the recirculation region. The numerical results demonstrate that the IMB method is effective to simulate the complex phenomena of flow passing bluff body and is easily extended to simulate moving or deformable bluff body in time varying flows.

ACKNOWLEDGEMENTS

This work was supported by the Hong Kong Polytechnic University (Project No. A-PB75, and ASD-A224).

REFERENCES

1. Peskin CS. Flow patterns around heart valves: A numerical method. *Journal of Computational Physics* 1972; **10**:252–271.
2. Goldstein D, Handler R, Sirovich L. Modeling a no-slip flow boundary with an external force field. *Journal of Computational Physics* 1993; **105**:354–366.
3. Saiki EM, Biringen S. Numerical simulation of a cylinder in uniform flow: application of a virtual boundary method. *Journal of Computational Physics* 1996; **123**:450–465.
4. Mohd-Yusof J. Combined immersed boundaries/B-Splines methods for simulations of flows in complex geometries. *CTR Annual research Brieds*, NASA Ames/Stanford University, 1997.
5. Kim J, Kim D, Choi H. An immersed-boundary finite-volume method for simulations of flow in complex geometries. *Journal of Computational Physics* 2001; **171**:132–150.
6. Fadlun EA, Verzicco R, Orlandi P, Mohd-Yusof J. Combined immersed-boundary finite-difference methods for three dimensional complex flow simulations. *Journal of Computational Physics* 2000; **161**:35–60.
7. Verzicco R, Orlandi P, Mohd-Yusof J, Haworth D. LES in complex geometries using boundary body forces. *AIAA Journal* 2000; **38**(3):427–433.
8. Lin P, Li CW. A σ-coordinate three-dimensional numerical model for surface wave propagation. *International Journal for Numerical Methods in Fluids* 2002; **38**:1045–1068.
9. Zhu L, Li CW. Error study on numerical approximation of radiation boundary condition for one-dimensional wave equation. *Communications in Numerical Methods in Engineering* 1993; **9**:475–482.
10. Li CW. Advection simulation by minimax-characteristics method. *Journal of Hydraulic Engineering* (ASCE) 1990; **116**(9):1138–1144.
11. Li CW, Lin P. A numerical study of three-dimensional wave interaction with a square cylinder. *Ocean Engineering* 2001; **28**:1545–1555.
12. Ferziger JH, Peric M. *Computational Methods for Fluid Dynamics* (2nd edn). Springer: Berlin, 1999; 389.
13. Van der Vorst HA, Sonneveld P. CGSTAB, a more smoothly converging variant of CGS. *Technical Report* 90-50, Delft University of Technology, 1990.
14. Grigoriadis DGE, Bartzis JG, Goulas A. LES of the flow past a rectangular cylinder using the immersed boundary concept. *International Journal for Numerical Methods in Fluids* 2003; **41**:615–632.
15. Lyn DA, Einav S, Rodi W, Park J-H. A laser-Doppler velocimetry study of ensemble-averaged characteristics of turbulent near wake of a square cylinder. *Journal of Fluid Mechanics* 1995; **304**:285–319.
16. Yu D, Kareem A. Numerical simulation of flow around rectangular prism. *Journal of Wind Engineering and Industrial Aerodynamics* 1997; **67–68**:195–208.
17. Rodi W. Comparison of LES and RANS calculations of the flow around bluff bodies. *Journal of Wind Engineering and Industrial Aerodynamics* 1997; **69–71**:55–75.
18. Bearman PW, Obasaju ED. An experimental study of pressure fluctuations on fixed and oscillation square-section cylinders. *Journal of Fluid Mechanics* 1982; **119**:297–321.
19. Lee BE. The effect of turbulence on the surface pressure field of a square prism. *Journal of Fluid Mechanics* 1975; **69**:263–282.
20. Rodi W. Large-eddy simulation of the flow past bluff bodies. In *Closure Strategies for Turbulent and Transitional Flows*, Launder BE, Sandham ND (eds). 2002; 361–391.
21. Norberg C. Flow around rectangular cylinders: pressure forces and wake frequencies. *Journal of Wind Engineering and Industrial Aerodynamics* 1993; **49**:187–196.
22. Cheng CM, Lu PC, Chen RH. Wind loads on square cylinder in homogeneous turbulent flows. *Journal of Wind Engineering and Industrial Aerodynamics* 1992; **41**;739–749.
23. Vickery BJ. Fluctuating lift and drag on a ling cylinder of square cross-section in a smooth and a in a turbulent stream. *Journal of Fluid Mechanics* 1966; **25**:481–494.
24. Durao DFG, Heitor MV, Pereira JCF. Measurements of turbulent and periodic flows around a square cross-section cylinder. *Experiments in Fluids* 1998; **6**:298–304.
25. Murakami S, Mochida A. On turbulent vortex shedding flow past 2D square cylinder predicted by CFD. *Journal of Wind Engineering and Industrial Aerodynamics* 1995; **54–55**:191–211.
26. Rodi W, Ferziger JH, Breuer M, Pourquie M. Status of large eddy simulation: results of a workshop. *Journal of Fluid Engineering* 1997; **119**:248–262.

